JOURNAL OF GEOPHYSICAL RESEARCH, VOL. 96, NO. C5, PAGES 8835–8852, MAY 15, 1991

Waves in Frazil and Pancake Ice and Their Detection in Seasat Synthetic Aperture Radar Imagery

PETER WADHAMS

Scott Polar Research Institute, University of Cambridge, Cambridge, England

BENJAMIN HOLT

Jet Propulsion Laboratory, California Institute of Technology, Pasadena

A theoretical model of waves propagating into an ice cover composed of frazil and pancake ice is developed and compared with measurements of wavelength and direction derived from synthetic aperture radar (SAR) imagery obtained from Seasat in October 1978. The theoretical model is based on the concept that ice of these types, which consists of small crystals or cakes, has only a mass-loading effect on the water surface. We derive the dispersion relation for phase and group velocities, finding that there is an upper frequency limit for propagation into the ice. From the reflection coefficient at the ice edge we derive the wave radiation pressure exerted on the ice, showing that it will cause a slick of frazil ice backed by thicker floes to become more dense or thick with increasing penetration. The implications for radar scattering enabling detection on SAR are that the Bragg resonant wavelength corresponds to waves above the frequency limit for propagation, so that a frazil slick appears dark on an SAR image. When the frazil ice becomes transformed into pancake ice, through slick compression or other means, the raised edges of the pancakes cause the ice to appear bright despite the fact that there are no waves present at the Bragg wavelength. These results are applied to a Seasat SAR image obtained from the Chukchi Sea. The appearance of the ice in the image corresponds to what we expect for frazil ice gradually transforming itself into pancake ice, backed by thicker floes. We derive directional wave number spectra outside and inside the ice cover by digital Fourier analysis of image subscenes, and we find that the change of wavelength and angle of refraction of the dominant wave entering the ice field are both characteristic of the dispersion relation derived theoretically. Mean ice thicknesses extracted from the theory correspond to thicknesses expected for such slicks. The technique offers a possible means of extracting the thickness of fields of frazil and pancake ice from SAR imagery; this may be of considerable utility when ERS 1 SAR is used to study the advancing winter ice edge in the Antarctic, which consists of vast areas of these ice types.

1. Introduction

Synthetic aperture radar (SAR) has been found to be capable of detecting ocean waves and swell within a sea ice cover. Observations to date have been made using airborne *X* band SAR [*Lyzenga et al.*, 1985] and C band SAR [*Carsey et al.*, 1989; *Raney et al.*, 1989; *Liu et al.*, 1991] in marginal ice zones comprising ice floes tens of meters in diameter. A very important component of the ice edge region, however, is pancake ice, which is composed of much smaller cakes and which is often associated with, or arises from, frazil ice, a suspension of small ice crystals in water. A key reason for its importance is that observations from the Antarctic pack ice in winter [*Wadhams et al.*, 1987; *Lange et al.*, 1989] suggest that the circumpolar Antarctic ice margin during the period of winter advance is composed of pancake ice to a distance of some 270 km from the ice edge, making pancake ice a major component of the ice cover. The advent of the ERS 1 satellite, equipped with a C band SAR, will enable this region to be routinely monitored from 1991 onward.

Fortunately, a single data set exists in which a satellite-borne SAR obtained imagery of waves propagating through an ice field which we interpret as being frazil and pancake ice. The data were obtained in the Chukchi Sea in October 1978 by the *L* band SAR on the Seasat satellite. In this paper we develop a theory for the propagation of waves in frazil or pancake ice and use it to interpret the nature of the imagery and the changes in wavelength and angle observed in the ice.

Paper number 91JC00457.
0148-0227/91/91JC-00457$05.00

2. Frazil and Pancake Ice

Frazil ice, a suspension of fine spicules or platelets of ice in water, is the initial ice type which forms on a sea surface in a region of high turbulence, such as the open ocean, the marginal ice zone, or a lead in which short waves are being generated by the wind. As growth proceeds, the suspension develops into a dense soupy slurry with ice concentration by volume of some 20–40% [*Martin and Kauffman*, 1981]. In this slurry the individual frazil platelets become sintered together to some extent to form flocs or clumps. This more developed ice type is called grease ice [*Armstrong et al.*, 1966]. Since there is a continuity between frazil and grease ice properties, we shall use the term "frazil ice" to describe both types. *Martin* [1981] has reviewed the properties of frazil ice in rivers and oceans, and a study of the frazil growth process was carried out by *Tsang and Hanley* [1985].

When a frazil ice suspension reaches a high enough concentration, it may accrete into cakes, typically 1 m across, called pancake ice. The pancakes acquire raised rims through the pumping of water or frazil ice onto their edges during collisions. The presence of wave energy is important at this time in preventing a large continuous sheet of nilas from forming, in determining the size of the pancakes, and in causing the collisions which produce the raised edges.

Pancake ice tends to be formed from large fields of frazil, since smaller areas of frazil which form in leads often get swept under the neighboring floe edges, to be deposited on floe bottoms as a layer of small randomly oriented crystals which then becomes part of the fabric of the floe. Such layers are common in ice cores recovered from the Antarctic [*Gow et al.*, 1982], where observations in winter show that pancake ice exists within a matrix of frazil, the freezing of which is the eventual cause of the formation of a coherent ice sheet [*Wadhams et al.*, 1987]. Figure 1 shows typical examples of frazil and pancake ice.

A third ice type with which we will be concerned is brash ice, an agglomeration of small broken-up pieces of ice, often in a matrix of frazil, which is found between floes in the marginal ice zone or in a distinct layer 1 km or more wide at the extreme ice edge under an on-ice wind. The pieces are broken from larger floes during wave-induced collisions, or else they are the remnants of floes which have broken up during the last stages of melt.

Martin and Kauffman [1981] made field and laboratory studies of frazil ice slicks in a wave field, in which they demonstrated a viscous damping mechanism for waves within the slick. They showed how wave herding of a slick against a floe edge can cause sufficient compression of the slick to accomplish the frazil-pancake transition. Finally, they showed how frazil ice slicks in the open sea tend to get wind-herded into Langmuir plumes by atmospheric roll vortices.

Martin and Kauffman considered only mechanisms of wave decay within the slick and assumed that this decay gives the internal compressive force required to accomplish the frazil-pancake transition. In this paper we consider the nature of the dispersion relation for gravity waves in a frazil ice slick, and we show that high-frequency waves cannot propagate in frazil ice and are therefore reflected at the slick edge. This total reflection, together with the partial reflection of lower-frequency waves at the edge, generates a wave radiation pressure along the slick's leading edge which is an important factor in the downwave herding of the slick. We also show that this rejection of high-frequency waves is important for the detection of frazil ice in SAR imagery, since there is no energy present at the Bragg wavelength so that frazil ice appears dark. Pancake ice will appear bright in SAR because of backscatter from the raised rims around the pancakes. We show that it is possible to detect the altered wavelength of swell in frazil and pancake ice by two-dimensional digital Fourier analysis of SAR images, with a Seasat image as a case study. We show that enhanced wave steepness within the ice field causes waves in some cases to show up more clearly within ice than in open water. Finally, we show that brash ice, too, when "seen" by a long swell, behaves like frazil and pancake ice, causing shortening and steepening of the swell as an initial effect before attenuation becomes important.

3. THE THEORY OF WAVE PROPAGATION IN FRAZIL ICE

3.1. *Dispersion Relation*

Consider a frazil ice slick of thickness h with a relative ice concentration c (fraction of the slick volume occupied by ice crystals). Let ρ_i and ρ_w be the densities of the ice and near-surface water, respectively. We assume for simplicity that the thickness is uniform so that the leading edge is a step (Figure 2); *Martin and Kauffman* [1981] found that in real wave-herded slicks the thickness increases steadily from zero at the leading edge to an equilibrium value in the interior. Water depth D is assumed to be large compared to the wavelengths of ocean waves that are present.

We first consider waves incident normally on the edge. In the ice-free region, if we assume inviscid, irrotational, and incompressible water motion, there is a velocity potential $\phi_n (n = 1, 2)$ obeying Laplace's equation

$$\nabla^2 \phi_n = 0 \tag{1}$$

with the boundary condition

$$\frac{\partial \phi_n}{\partial y} = 0 \Big|_{y=D} \tag{2}$$

In region 1 (Figure 2), let $\eta_1(x, t)$ be the instantaneous elevation of the water surface. Then by the linearized Bernoulli equation for a free surface,

$$\eta_1 = -\frac{1}{g} \frac{\partial \phi}{\partial t} \Big|_{y=0} \tag{3}$$

with the kinematic surface boundary condition

$$\frac{\partial \eta_1}{\partial t} = -\frac{\partial \phi_1}{\partial y} \Big|_{y=0} \tag{4}$$

For a monotonic wave of angular frequency ω and wavelength λ proceeding in the x direction, a solution of (1)–(4) is

$$\phi_1 = [Be^{ikx} + Re^{-ikx}]e^{-ky}e^{-i\omega t} \tag{5}$$

where $k = 2\pi/\lambda = \omega^2/g$ if $D \gg \lambda$. $|B|$ and $|R|$ are the potential amplitudes of a wave incident on the leading edge of the slick and a wave reflected normally from the leading edge.

In region 2, let $\eta_2(x, t)$ be the instantaneous elevation of the slick surface. Assuming that the slick does not deform under wave action, this is also the vertical displacement of the slick-water interface. The equation of motion of the slick is

$$p(x, t) = \rho_i ch \frac{\partial^2 \eta_2}{\partial t^2} \tag{6}$$

where $p(x,t)$ is the pressure just below the slick-water interface. This assumes that the suspension is equivalent simply to a mass loading of the water surface, without any spatial coherence or internal stress within the slick.

Applying the linearized Bernoulli equation to the slick-water interface gives

$$p(x, t) = -\rho_w \left[g\eta_2 + \frac{\partial \phi}{\partial t} \Big|_{y=0} \right] \tag{7}$$

The boundary condition for velocity potential under the slick is

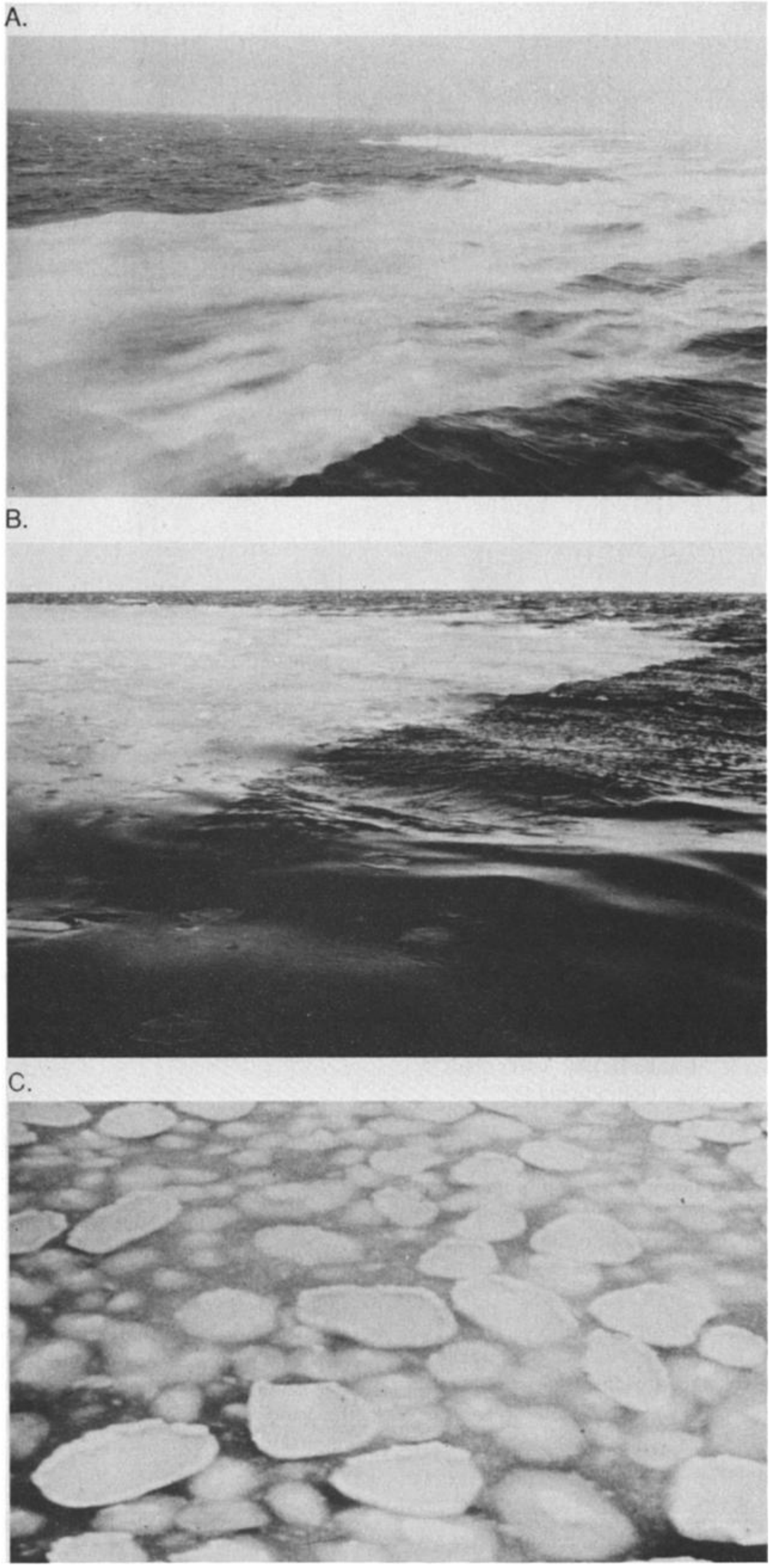

Fig. 1. Photographs of (*a*) a frazil ice slick in the open sea, (*b*) a frazil slick which also contains pancake ice, and (*c*) a field of pancake ice in a frazil ice suspension (typical pancake diameter 1–2 m).

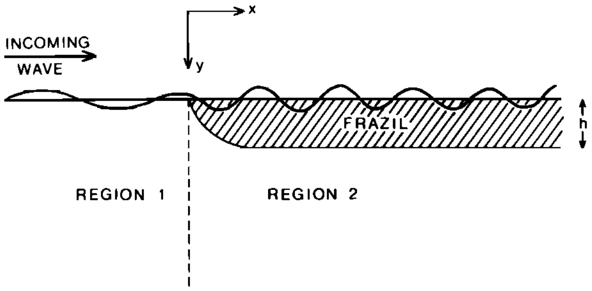

Fig. 2. Diagram of frazil ice being herded by waves [after *Martin and Kauffman*, 1981].

$$-\left.\frac{\partial \phi_2}{\partial y}\right|_{y=0} = \frac{\partial \eta_2}{\partial t} \tag{8}$$

A solution of (6)–(8) is

$$\phi_2 = \sum [A_n \exp(ik_n x) + B_n \exp(-ik_n x)] \cdot \exp(-k_n y) \exp(-i\omega t) \tag{9}$$

where

$$k_n = \frac{\rho_w \omega^2}{\rho_w g - \rho_i c h \omega^2} = \frac{k}{1 - chk\rho_i/\rho_w} \tag{10}$$

Thus a wave can propagate in the slick, but with the reduced wavelength $\lambda_i = 2\pi/k_n$. The properties of such a wave are as follows.

1. Its phase velocity is less than in open water, so that waves incident obliquely on the slick are refracted toward the normal. For an angle of incidence θ_1 the angle of refraction θ_2 is given by Snell's law:

$$\sin \theta_2 = \frac{k \sin \theta_1}{k_n} \tag{11}$$

2. The group velocity U_i in the slick is lower than its value U_w in open water, the relationship being

$$U_i/U_w = k^2/k_n^2 \tag{12}$$

This implies that the wave has an increased amplitude within the ice. Assuming perfect energy transmission, we can equate energy fluxes in open water and in the slick to find that the amplitude A_i of a wave in the slick is related to its amplitude A_w in open water by

$$A_i^2/A_\omega^2 = U_w/U_i = k_n^2/k^2 \tag{13}$$

3. Most importantly, for the present study, there is a frequency limit given by

$$\omega_c = \left[\frac{\rho_w g}{\rho_i c h}\right]^{1/2} \tag{14}$$

above which propagation is not physically possible. A wave incident normally at a higher frequency than ω_c will suffer total reflection at the ice edge. This will occur even if the slick edge is not a sharp step as in Figure 2 but is more gently inclined, so long as h and c are the final ice thickness and concentration. For typical values of $c = 0.3$, $h = 1$ m, $\rho_i = 900$ kg m^{-3}, and $\rho_w = 1025$ kg m^{-3}, we obtain $\omega_c = 5.72$,

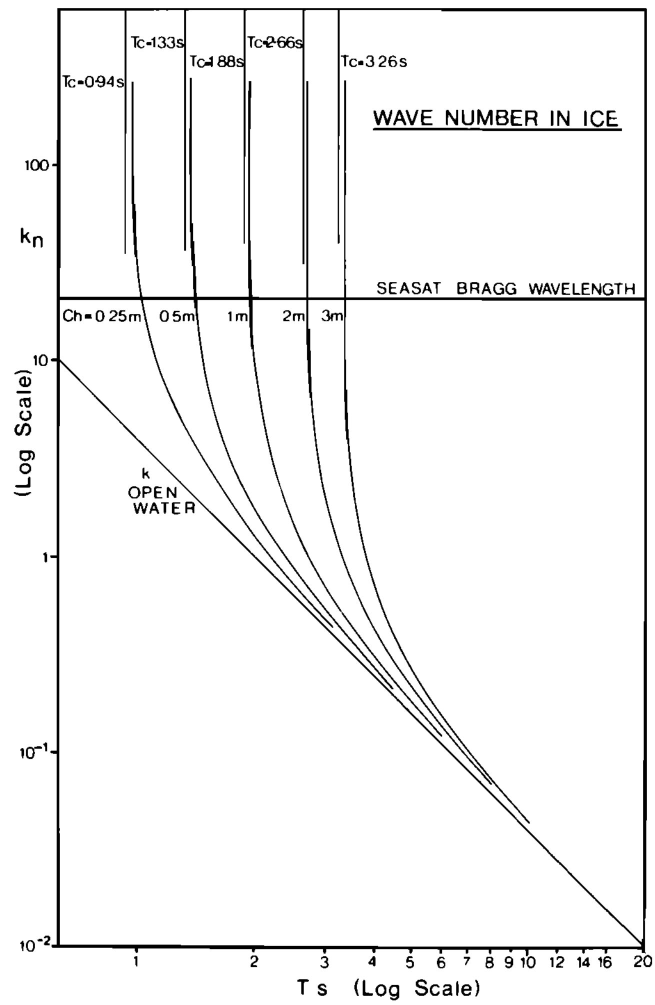

Fig. 3. The wave number k_n in ice as a function of wave period for different ice thicknesses. In each case the critical wave period T_c for propagation in ice is shown, as well as the Bragg wavelength for the Seasat SAR.

corresponding to a frequency of 0.91 Hz and wave period 1.1 s.

Figure 3 shows k_n as a function of frequency for various values of (ch). The lower (ch) values of 0.25 and 0.5 m correspond to typical frazil ice slick equivalent thicknesses, while the higher ranges of 1, 2, and 3 m are appropriate to brash ice where $c \simeq 1$ and h is the mean thickness of the ice blocks. It can be seen that k_n drops rapidly toward k as the wave period increases beyond T_c. If we regard a wavelength change of 20% or more as representing a significant change in the wave propagation characteristics, then the range of wave periods for which $k_n/k > 1.2$ is as follows:

(ch), m	T_c, s	Maximum Period for $k_n/k > 1.2$, s
0.25	0.94	2.4
0.5	1.33	3.3
1	1.88	4.6
2	2.66	6.6
3	3.26	8.0

Swell therefore passes through both frazil and brash ice with almost no change in its properties; long wind waves are affected by brash but not by frazil; shorter wind waves are affected by frazil ice and may be completely rejected by brash ice; and the shortest gravity and capillary waves are rejected by frazil ice.

3.2. *Reflection and Transmission*

The transmission of waves into an ice field of this kind was studied by *Weitz and Keller* [1950] and by *Peters* [1950]. Weitz and Keller considered a wave incident on the ice edge at an angle θ to the normal such that

$$k_y = (2\pi \sin \theta)/\lambda \tag{15}$$

and solved for ϕ_2 using a Green's function. In a later paper [*Keller and Weitz*, 1953] they were able to simplify their solution to

$$|R| = \left| \frac{(k^2 - k_y^2)^{1/2} - (k_n^2 - k_y^2)^{1/2}}{(k^2 - k_y^2)^{1/2} + (k_n^2 - k_y^2)^{1/2}} \right|_{\omega < \omega_c} \tag{16}$$

where $|R|$ is the amplitude reflection coefficient. The amplitude transmission coefficient $|T|$ was obtained by *Shapiro and Simpson* [1953], who showed that

$$1 - |R|^2 = |T|^2 k/k_n \tag{17}$$

giving, in the case of normal incidence,

$$|T| = 2k_n/(k_n + k) \tag{18}$$

Figure 4 shows $|R|^2$ and $|T|$ as a function of period for various values of (ch) at normal incidence. It can be seen that $|R|^2$ rapidly drops to a low value as the frequency drops below ω_c, so that the main reflection effect is the total reflection which occurs above ω_c. $|T|$ is the ratio of amplitude within the ice to amplitude in open water, taking account of reflection, and it can be seen that this ratio rises to a high value near ω_c, corresponding to very low values of group and phase velocity. An incoming wave of frequency just below ω_c therefore enters the slick with a much reduced wavelength and greater amplitude. This bunching of energy near the leading edge of the slick gives an opportunity for internal decay mechanisms, such as the viscous effect found by *Martin and Kauffman* [1981], to be very effective in attenuating the wave. We therefore expect waves which have a high value of $|T|$ not to propagate very far into a frazil ice slick.

Figure 5 shows the effect of oblique incidence on $|R|^2$. Transmission into the ice is most efficient at normal incidence, but the effect of oblique incidence is not strong except near grazing incidence, where waves which are transmitted almost perfectly at most angles (for example, with $ch = 0.25$, $T = 10$ s) begin to suffer large reflections.

3.3. *Wave Radiation Pressure*

A wave which is partly or wholly reflected at a boundary between two media imparts a stress on that boundary which is called the wave radiation pressure [*Longuet-Higgins*, 1977]. A wave of amplitude a, phase velocity C, and group velocity U has an average horizontal momentum due to the mass transport velocity of

$$I = \rho_w g a^2/2C \tag{19}$$

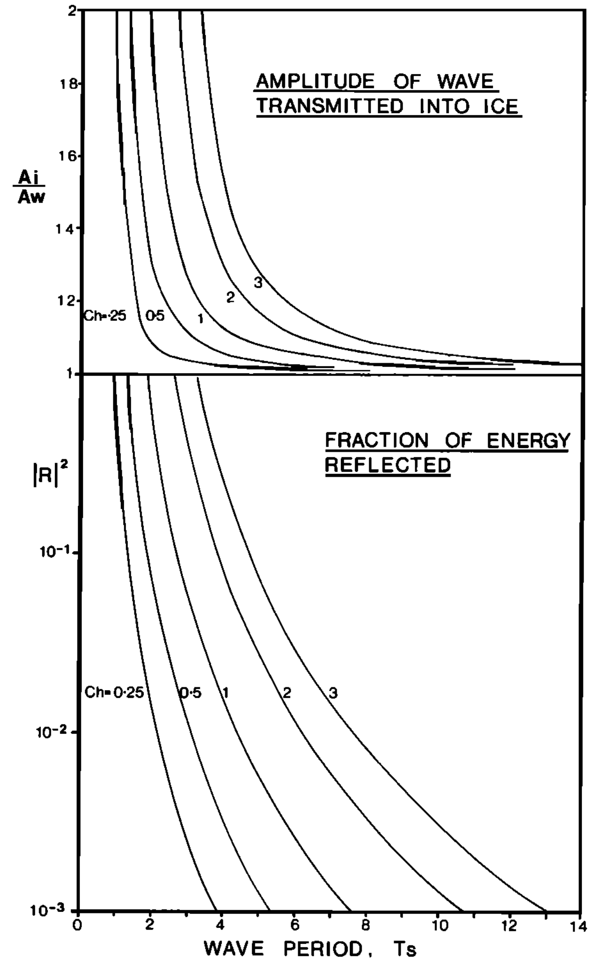

Fig. 4. (Top) Ratio of amplitude of a wave transmitted into ice to amplitude of the same wave when in open water, as function of wave period for different ice thicknesses. (Bottom) The fraction of normally incident wave energy reflected from the ice edge back into the open sea as function of wave period for different ice thicknesses.

which gives a momentum flux of $(\rho_w g a^2 U/2C)$. The change of momentum flux across the slick boundary is equal to a force F per unit length of wave front exerted on the boundary. Consider normal incidence, for simplicity, and let A_i, A_r, and A_t be the amplitudes of the incident, reflected, and transmitted waves, respectively, with $U_i(= \partial\omega/\partial k_n)$, C_i, $U_w(= \partial\omega/\partial k)$, and C_w as the group and phase velocities in open water and in the ice slick. The wave radiation pressure is then

$$F = \frac{\rho_w g}{2}\left[\frac{A_i^2 U_w}{C_w} + \frac{A_r^2 U_w}{C_w} - \frac{A_t^2 U_t}{C_i}\right] \tag{20}$$

which from (12), (13), (16), and (18) yields

$$F = \frac{\rho_w g A_i^2 (k_n - k)^2}{2(k_n + k)^2} \tag{21}$$

The effect of this force on the slick boundary depends on the nature of the material in the slick and on the position of the slick. Three distinct cases which can be distinguished are as follows.

1. For a slick of frazil ice, freely floating in the open sea (Figure 1*a*), a compressive force on the leading edge will

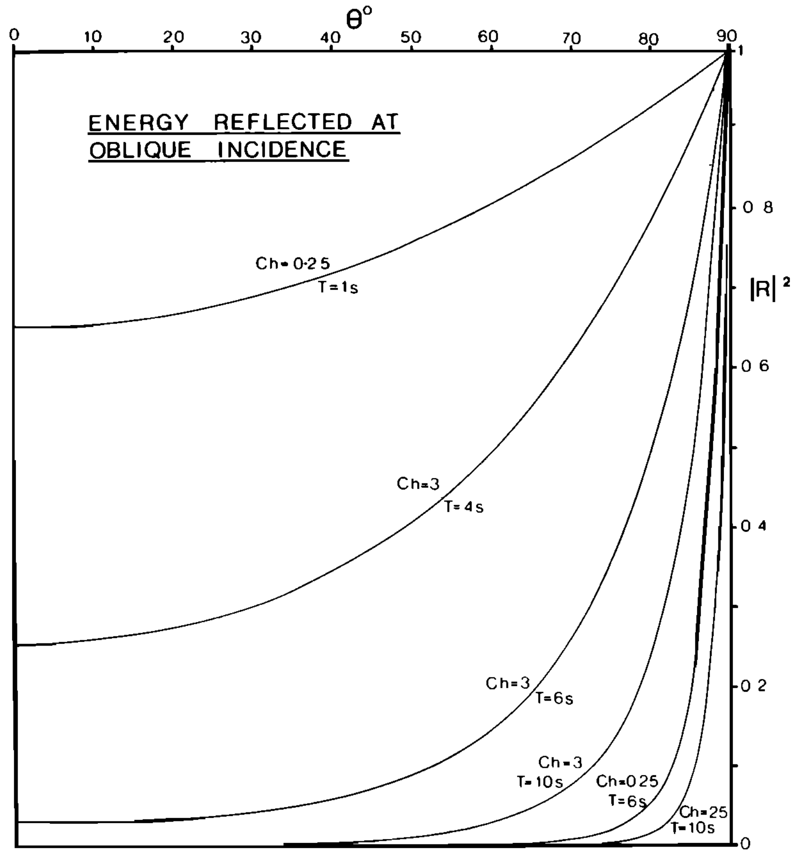

Fig. 5. Fraction of incident wave energy reflected back into the open sea when the wave is incident at angle θ, for various wave periods and ice thicknesses.

cause the slick initially to become narrower as the ice suspension thickens and/or becomes more concentrated. Eventually, the tendency of the ice slurry to slump outward under its own buoyancy will balance F, and the slick will then move bodily to leeward under the effect of F. Thus F both drives the slick and helps keep it coherent and compacted.

2. If the slick is of frazil ice backed by thicker floes, for example, a slick lying just outside a main ice edge with an on-ice wind, F will cause the slick to thicken and/or become more concentrated as in case 1. However, the "fixed" leeward boundary will force a much greater compaction than in case 1 and will tend to produce a zone of no motion near itself, allowing the slick to cohere into pancake ice or even nilas at its leeward end. This effect was studied observationally and experimentally by *Martin and Kauffman* [1981].

3. If the slick is of brash ice, it may have sufficient strength to resist deformation under F, so that F is transmitted through the brash ice as a compressive stress. Under these circumstances, *Mollo-Christensen* [1983] has shown that the compressive stress will itself produce a further decrease of group velocity within the brash ice. His result for the simplified case where $kh \ll 1$ and $c = 1$ is

$$U_t \simeq 2^{-1}(g/k)^{1/2}[1 - 2Fhk^2/(\rho_w g)] \qquad (22)$$

The effects of the ice on the wave (decreased group and phase velocity, decreased wavelength, increased amplitude, wave rejection above a critical frequency) are therefore amplified still further by the compressive stress. It should be noted that only a restricted ice type fulfills the conditions of Mollo-Christensen; it must be a field of brash ice possessing blocks of small spatial dimensions in relation to wavelength (so that scattering does not become the dominant effect), but of a thickness and uniformity sufficient to give the ice field some strength under compression.

In the next section, we examine the implications of frazil ice rejecting high-frequency waves on SAR wave imaging, since the appearance of waves on radar imagery is directly related to the small-scale wave components. Next we proceed with the analysis of the SAR imagery itself and finally compare the wave measurements with the theory.

4. Implications for SAR Detection

The precise mechanisms by which synthetic aperture radar interacts with the sea surface to produce a resulting image are not well understood and are still the subject of active research [e.g., *Alpers*, 1983; *Alpers and Bruening*, 1986; *Beal et al.*, 1986; *Monaldo and Lyzenga*, 1988]. It appears, however, that three mechanisms are of especial importance:

1. Bragg resonance is important, whereby the incident radar waves are backscattered by that short-wave component of the surface roughness whose wavelength matches that of the radar waves on the sea surface and which therefore gives a coherent return. The Bragg resonant wavelength λ_w is given by

$$\lambda_w = \lambda_{radar}/(2 \sin \Psi) \tag{23}$$

where Ψ is the incidence angle. The Seasat SAR was an L band instrument operating at 1.275 GHz. Its wavelength, λ_{radar}, was 23.5 cm, and the incidence angle was 23° ± 3°, giving $\lambda_w = 30 \pm 4$ cm. These short-wave components may be tilted according to the local slope of a longer wave. Radar backscatter is produced when the short waves are tilted toward the radar.

2. The short Bragg waves are modulated by the local long-wave orbital velocity which varies with position along the wave. The Bragg resonant waves are amplified on the crests of a swell and attenuated in their troughs. This results in periodic modulations in image intensity for swell in the presence of a wind sea.

3. Velocity bunching, a mechanism invoked by *Lyzenga et al.* [1985] to explain the unusually clear imaging of waves in ice fields, is also important. This is a periodic increase and decrease in image intensity within a homogeneous area of ice or water caused by the radial component of wave orbital velocity. It is offset in the open sea by the random motion of shorter waves, not present in the ice, which affect the coherence time limitation. In ice fields the coherent motion of the floes at the wave orbital velocity enables the velocity-bunching effect to operate at its full potential.

The implications of these mechanisms for the detection of waves in frazil ice, and for the detection of frazil ice itself, are profound. In Figure 3 we have shown the wave number corresponding to the Seasat λ_w. It cuts the k_n curves at periods just above T_c, and in fact so close to T_c that waves of the relevant frequencies (a different frequency for each ch value) suffer extreme modification on passage across the ice edge. Consider, for instance, a frazil ice slick where ch = 0.25 m, for example, a slick 1 m thick with a 25% ice concentration within it. Figure 3 shows that Bragg waves within this slick have a period of 1.05 s, and Figure 4 (or the relevant equations) shows that a wave of this period passing into the slick from the open sea suffers a 54% reflection of energy at the edge of the slick, and that the wave transmitted into the slick has a group velocity of only 0.03 of its open water value and an amplitude in ice of 4.4 times its open water value. Such a steep, slow-moving wave will be rapidly attenuated by viscous mechanisms very close to the edge of the slick and will not propagate into the body of the slick. The slick will therefore appear smooth at Bragg wavelengths and will look dark on SAR imagery.

The same argument applies to pancake ice, where (ch) lies in the range of 0.25–0.5 m. However, while a suspension of minute ice crystals in water does not disturb a smooth water surface, the raised edges of pancakes have a significant roughness at Bragg wavelengths. For this reason a region of pancake ice can be expected to appear bright on SAR imagery. There may also be a positive backscatter contribution due to a high surface salt content (which increases the dielectric constant) resulting from pumping of water and frazil ice onto the surface during collisions, but this increase would be offset by any actual surface wetness present. We would hope, in the case of frazil slicks lying against ice edges, to see the phenomenon mentioned in case 2 above, i.e., a frazil slick transforming at increasing downwave distance into pancake ice. This would reveal itself as a dark area gradually becoming bright with increasing distance from the leading edge.

Finally, we might expect wind waves to be more clearly visible in pancake or brash ice (but perhaps not in frazil, because of the overall dark image) than in the open sea. This is because the increase in wave steepness (greater amplitude and shorter wavelength), when not so extreme as to cause the wave to decay rapidly, may be sufficient to increase the slope modulation of the signal and so render the wave more clearly visible. We might hope to detect this change in wavelength from a Fourier analysis of the image.

5. THE SEASAT SAR IMAGERY

To test the proposed model for detecting changes in waves as they propagate through frazil and pancake ice, imagery from the Seasat SAR was selected that was obtained over the marginal ice zone in the Chukchi Sea approximately 150 km north of Wrangel Island [*Fu and Holt*, 1982]. The imagery was obtained on October 8, 1978, at 1547 UT during Seasat orbit 1482 (Figure 6). The satellite flight direction at the time of data acquisition was 245°. Two digitally processed images have been mosaicked to form a scene size of 100 km by 200 km. Seen in the image (Figure 6*a*), starting from the bottom, is open ocean (gray) followed by an extensive area of frazil ice (dark) which develops into brightly appearing pancake ice near the top. The edge of the solid pack ice is in the upper right corner and appears moderately gray. A zone of brash ice is compacted against the pack ice and has a distinct bright outer edge. The incoming waves are propagating northwest and are seen most clearly in the pancake ice region and also in the narrow zone of brash ice against the solid pack. These interpretations are based on the arguments given in the section above and are in fact confirmed by simultaneous Seasat passive microwave radiometer data over the same region of the SAR imagery which shows brightness temperatures characteristic of young first-year ice [*Carsey and Pihos*, 1989, Figure 14]. Other SAR studies that generally support these interpretations of frazil and pancake ice include those of *Johannessen et al.* [1983] and *Sutherland et al.* [1989].

Briefly, the Seasat SAR system operated at a frequency of 1.275 GHz (L band, 23.5 cm), a fixed center incidence angle of 23°, and a spatial resolution of 25 by 25 m in range and azimuth and had a swath width of 100 km. The imagery has a relatively narrow range of incidence angles from 20° to 26° across the 100-km swath. Both images were processed to four looks with ground range correction to remove skewness in the azimuth direction which results from Earth rotation while the radar is operating.

Seen in Figure 6*b* are the locations of the subscenes selected for wave analysis. The subscenes were selected (1) to contain a relatively homogeneous zone of ice (i.e., frazil, pancake, brash) depending on both the image tonal level and texture patterns and (2) to be along a line nearly parallel to the general propagation direction of the incoming open ocean wave field in order to trace the transformation of the waves in the ice. The boxes are numbered 1–29 and define six lines into the ice (A–F), while box 30 is of open water away from the ice zone. Most of the selected subscenes were 6.4 by 6.4 km in size except for a few that were 3.2 by 3.2 km, necessitated by a small zone of homogeneous ice. Figure 6*c* shows the location of the image in relation to bathymetry.

Figure 7 shows enlargements of subscenes along line A

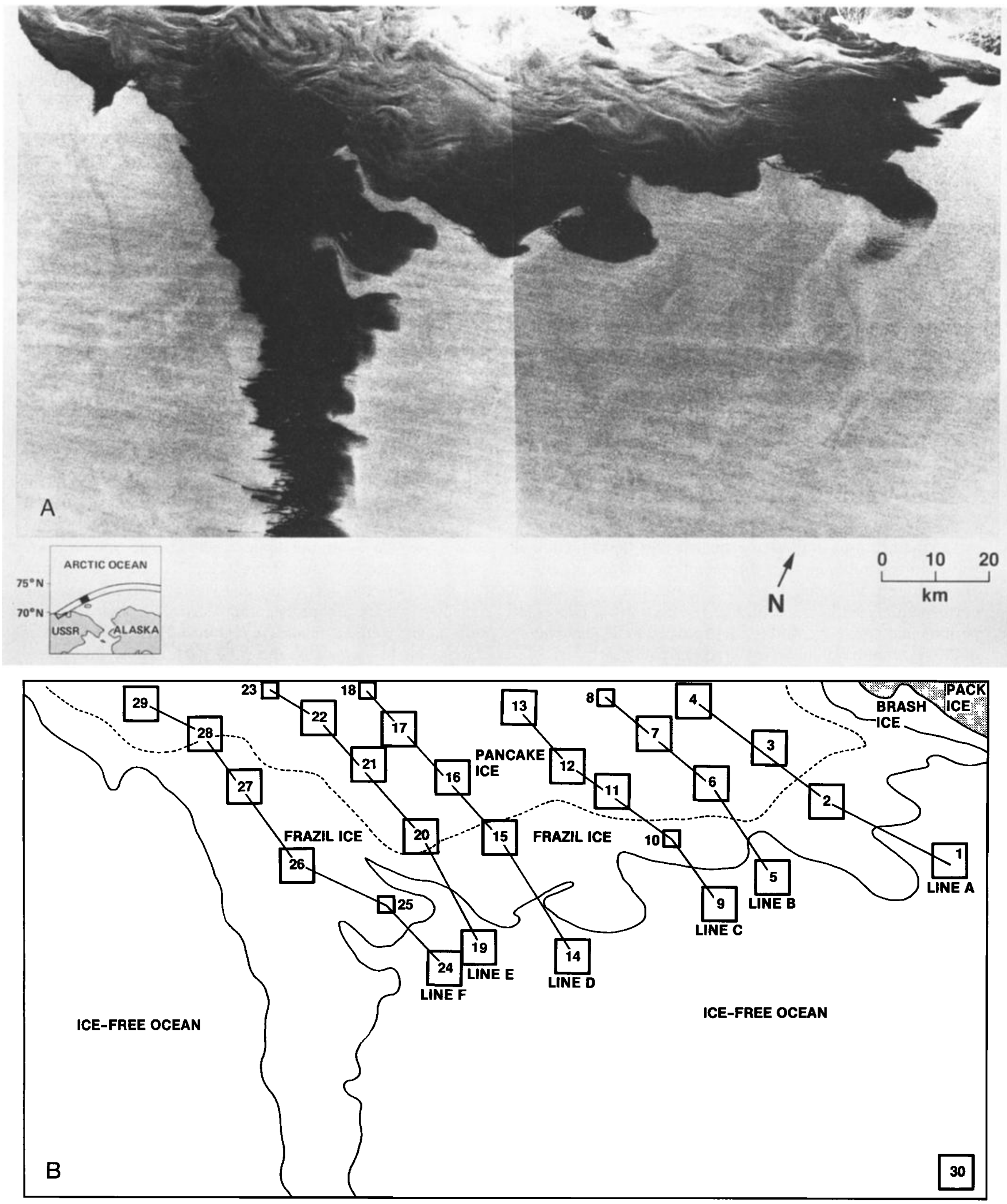

Fig. 6. (*a*) Seasat SAR imagery of the Chukchi Sea taken October 8, 1978, at 1547 UT, (*b*) a sketch map indicating the major zones of open ocean and ice and the location of subscenes used for deriving the wave measurements, and (*c*) a detailed bathymetry map of the Chukchi Sea with the location of SAR imagery indicated. The contour intervals are 10 m. The map was compiled from *Perry and Fleming* [1986].

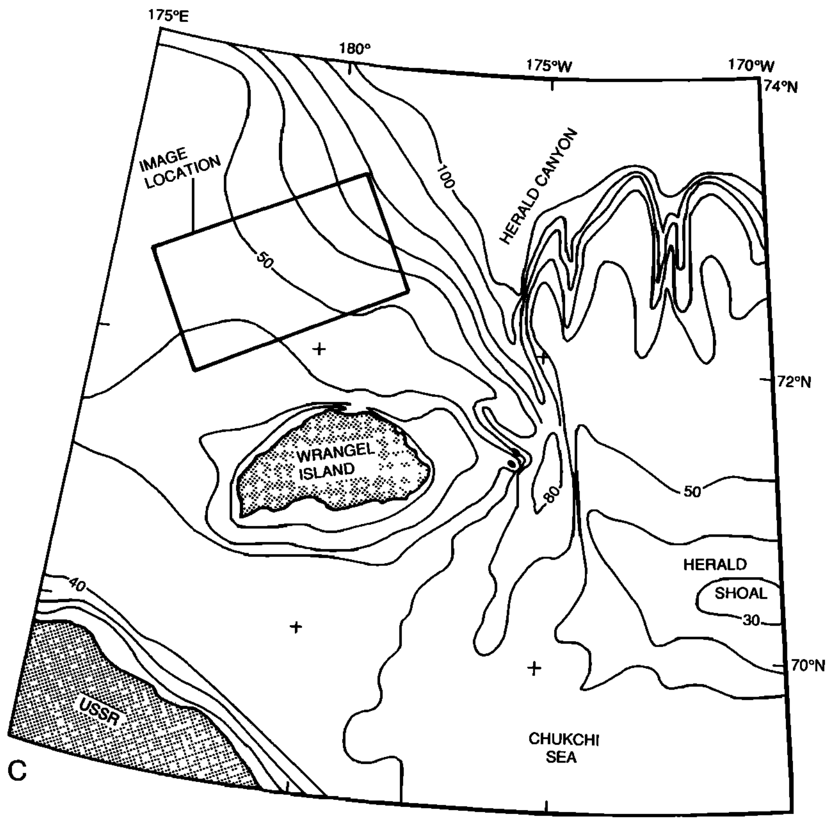

Fig. 6. (continued)

and line E from Figure 6 to enable closer examination of the imaging characteristics. For line A, box 1 is open ocean which appears uniformly bright because of wind roughening. Waves are visible as periodic modulations, characteristic of the appearance of surface waves on SAR. Box 2 contains darkly appearing frazil ice. Note the absence of clearly visible surface waves in the subscene, which is the case for the remaining frazil ice areas. Both the low return from the frazil ice and the absence of visible waves are due to damping of the high-frequency wave components by the new ice. Near the ice-ocean margin the frazil ice can be seen aligned into bands (Figure 6). The bands are formed by Langmuir circulation and are known to line up parallel to the wind direction [*Martin and Kauffman*, 1981]. The bands are aligned roughly parallel to the platform flight direction (245°). Boxes 3 and 4 show the next ice zone where the ice becomes increasingly bright toward the north with swirling streaks often present. The swirling patterns indicate that the ice field is composed of unconsolidated small cakes which are subject to local forcing by current and wind. Surface waves are seen particularly well in this zone propagating along a northwest/southeast direction. This zone is most likely composed of pancake ice which develops from frazil ice when it reaches a suitable concentration. The raised rims of the pancakes act as corner reflectors to the incoming radar signal. The gradually increasing brightness is most likely due to a combination of the increasing concentration of pancakes (and therefore increasing number of raised rims within a given area) plus the increasing size and roughness.

Enlargements for subscenes in line E are included in Figure 7 because this ice has a slightly different appearance from lines A–D. This affects the wave dispersion results, as will be discussed in section 6. Box 19 is over the open ocean. Boxes 20–23 contain pancake ice which is not as bright as in boxes 3 and 4, for example, and does not vary as rapidly with increasing distance from open water as the pancake ice seen in lines A–D.

Surface weather analyses of this region were obtained from the National Weather Service (NWS) and the Navy through the National Center for Atmospheric Research. The NWS analysis indicates air temperatures near 0°C and low winds on October 5–6. At Wrangel Island, located 100 km south of the imagery, from October 7 up to the time of the Seasat pass on October 8, the easterly winds increased in speed to 8–11 m s^{-1}, and the air temperatures cooled to below −4°C. The increased winds were due to a low-pressure system located over the Gulf of Alaska which deepened significantly as it moved northward against the high-pressure zone centered over the Arctic, resulting in strong geostrophic winds with considerable fetch that blew steadily westward across the northern Alaskan coast and the Chukchi Sea. At the time of the overpass the winds measured at Wrangel Island were 11 m s^{-1} from a direction of about 50°. The Navy surface analysis is formatted into approximately 400 km by 400 km grids. Overall, the Navy analysis generally confirms the NWS analysis for those grid points nearest to the imagery location. From October 5 to the time of the overpass on October 8, air temperatures decreased to about −4°C with lower temperatures (about −7°C) to the east, wind speeds increased from 5 to 12 m s^{-1}, and the wind direction rotated from about 120° to 60°.

Significant wave height (H_s) data were obtained from the

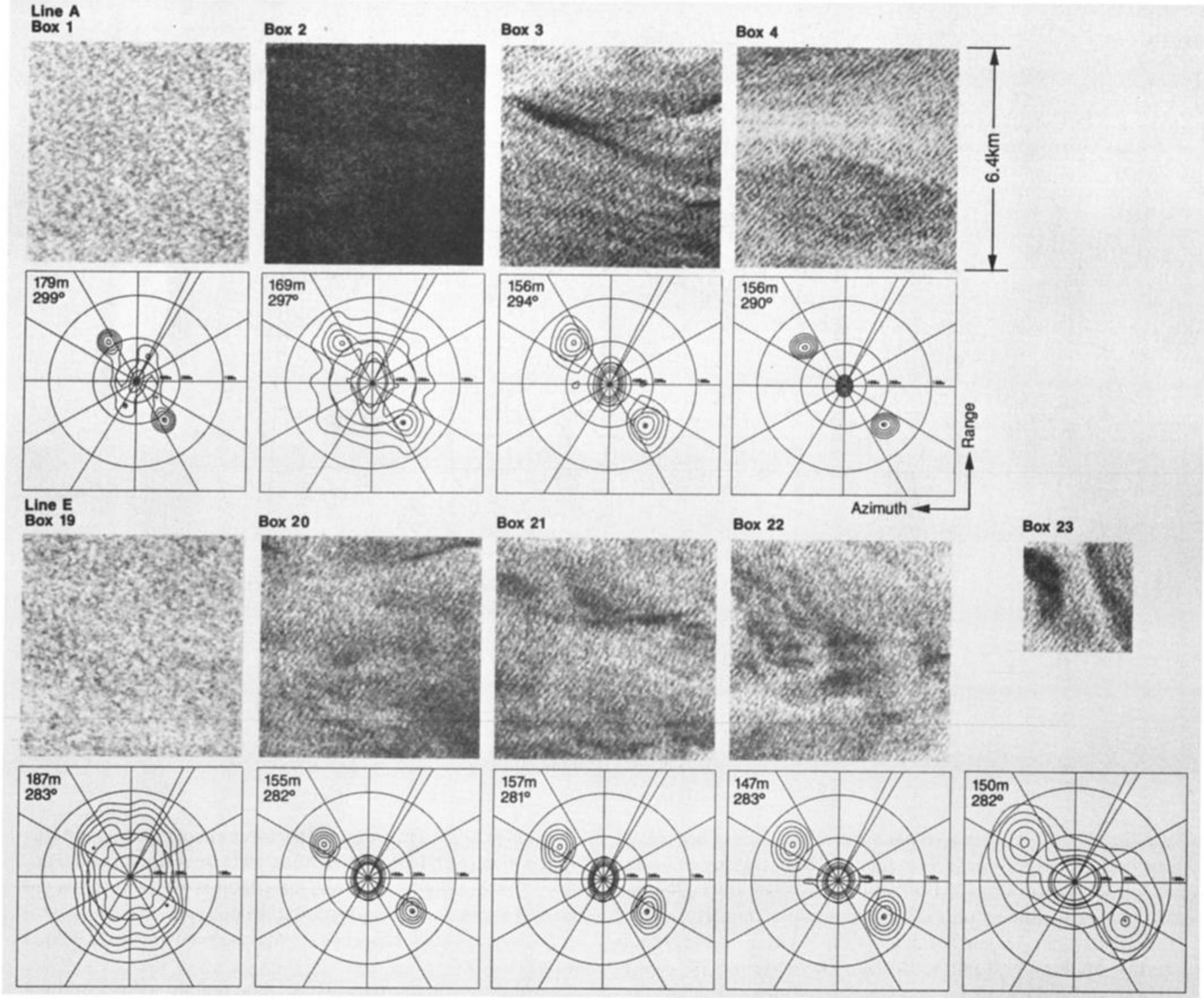

Fig. 7. Enlargements of SAR imagery for line A (boxes 1–4) and line E (boxes 19–23) with the corresponding wave spectral contour plot below each subscene. The wavelength and direction are indicated for each contour plot. The surface waves are clearly visible as periodic modulations in each image.

Seasat altimeter for the ice-free portion of the Chukchi Sea for the period from October 5 to October 8. These data extend only as far as 72° on any given track because of the Seasat orbital inclination (108°). From October 6 to October 7, H_s increased from 1 m to about 3 m. On October 8, altimeter data were obtained from three separate passes each 100 min apart in time: 1482, 1483, and 1484, with pass 1483 being the closest to the image location in Figure 6. Each pass indicated H_s of between 4 and 5 m in the vicinity of the imagery, with an average of about 4.5 m. These measurements were obtained over ice-free areas of considerable extent since the presence of the ice edge is easily distinguishable in the wave output. The increase in H_s coincides with the presence of the strong easterly winds observed in the weather analysis.

The above analyses verify the presence of both the waves and the ice conditions seen in the radar imagery. A Seasat pass (orbit 1439) acquired on October 5 along the same orbital track as on October 8 showed a limited zone of frazil ice adjacent to a less compacted solid ice pack. While the temperatures measured at Wrangel Island were about −4°C at the time of the overpass, the actual air temperatures at the ice edge may have been lower because of local ice effects and as indicated by the lower temperatures to the east shown in the Navy analysis. The winds are nearly parallel in direction with the ice bands seen in Figure 6*a*, strongly suggesting that the ice bands are being aligned by the wind. However, the surface waves in the imagery are propagating in a direction that is rotated approximately 45° to the right of the geostrophic wind direction, indicating that the waves are not being affected by the local winds.

6. Analytical Method and Results

6.1. *Wave and Ice Measurements*

The wave measurements derived from the SAR imagery are listed in Table 1 for all 30 boxes (see Figure 6*b* for

TABLE 1. Wave and Ice Measurements From SAR Imagery

Box	Angle, °N	Wavelength, m	Distance, km	Class	Brightness Mean	Brightness Standard Deviation
1	298.7	178.7	0	1	159	30
2	297.1	169.3	25.5	2	48	13
3	293.6	155.7	40.2	4	121	41
4	289.6	156.1	57	5	186	47
5	294.0	173.5	0	1	155	29
6	288.6	164.5	21.1	4	127	39
7	286.6	158.6	35.3	5	156	46
8	282.0	149.5	46.5	5	159	48
9	297.8	182.9	0	1	156	29
10	···	···	15.3	2	28	11
11	287.6	161.5	29.3	4	115	35
12	286.6	158.6	39	4	120	37
13	283.7	155.2	52.9	5	150	46
14	287.3	180.9	0	1	151	27
15	288.6	164.5	26	2	24	18
16	282.6	157.6	40.3	3	96	32
17	280.6	156.8	53.9	3	102	39
18	282.0	149.5	65.4	4	119	41
19	282.5	187.1	0	1	150	29
20	281.8	154.6	23.6	3	60	27
21	280.6	156.8	40.4	3	79	31
22	283.1	147.4	53.3	3	89	34
23	282.0	149.5	63.8	3	94	37
24	···	···	0	1	149	30
25	···	···	16.5	2	4	11
26	···	···	34.7	2	1	5
27	276.3	160.2	52.7	2	20	13
28	275.6	156.8	65.2	3	54	25
29	278.3	147.9	78.3	3	88	29
30	291.6	180.9	0	1	163	30

locations). The open ocean boxes are defined to be at 0 km, and the distances for the remaining boxes in each line are referenced from those points. Box 30 is of the open ocean about 50 km away from the ice field. Also listed in the table are the mean and standard deviation of the brightness histograms and the type of ice for each box.

The measurements of the directional wave spectra were derived from the SAR imagery using a procedure described by *Holt et al.* [1990]. A two-dimensional digital fast Fourier transform (FFT) is obtained from each subscene (256 by 256 pixels, 25 m per pixel). The resulting unsmoothed spectral density estimate has a spectral resolution of $\Delta k = (1/128)2\pi/50$ rad m^{-1} = 0.001 rad m^{-1} and a chi-square distribution with 2 degrees of freedom [*Monaldo*, 1991]. To reduce sampling variability, each spectrum is smoothed using a moving Gaussian filter with a full width of 21 by 21 pixels and a kernel of 5 pixels. The smoothing increases the degrees of freedom to 164 on the basis of the effective area of the filter [*Beal et al.*, 1986]. A peak-finding routine then locates the dominant local maxima or wave peaks and determines the wavelength and direction of the peaks by their distance and orientation to the north. The wave spectra are displayed as contour plots, examples of which are shown in Figure 7 for lines A and E. Each plot has an inherent 180° ambiguity in wave direction due to the formatting of the plots. The ambiguity has been resolved by comparison with the wind directions indicated on the weather charts. Aside from the smoothing filter, no other corrections have been made to the SAR imagery for either system or modulation transfer functions.

The accuracy of the wave products are estimated from Figure 7 by *Monaldo* [1991], who shows the root-mean-square variation in wave number and propagation direction as a function of kernel size of the Gaussian filter, using a similar peak-finding routine as is incorporated here. These variations show a gradual increase in accuracy with increasing kernel size from zero to 4. Extrapolating this figure out to a kernel size of 5 results in a spectral precision of ±2° in propagation angle and ±0.002 rad m^{-1} in wave number. Over the approximate range of measured wavelengths (145–190 m), the accuracy in the wavelength estimates averages ±5.5%. The open ocean wave measurements and considerations for the possibility of nonlinearities in these data are discussed in section 6.2. The waves measured in the ice are discussed in section 6.3.

From the imagery it is clear that there is an evolution in the ice conditions from the formation of frazil ice to pancake ice over distance. In order to examine the changes in the wave properties with ice condition, histograms of the pixel brightness values were obtained from each of the 30 image subscenes. Before the histograms were obtained, the full-sized images underwent a stretching routine to raise the overall brightness level of the imagery and reduce the nonuniformity in radiometric brightness in image range which results from an incomplete knowledge of the radar antenna pattern and small changes in the backscatter for a given feature type with increasing incidence angle. This stretching procedure has no effect on the wave spectra measurements. An analysis of the histograms of the various ice classes and the effects of ice type on the wave measurements are discussed in section 6.4.

6.2. *Results of Open Ocean Wave Measurements*

Ocean wave spectra were obtained from boxes 1, 5, 9, 14, 19, 24, and 30. All ocean spectra contained discernible dominant wave peaks except box 24, where no definable peak was present. The mean wavelength for all boxes is 180.7 m with a standard deviation of 4.5 m. The mean propagation direction is 292° with a standard deviation of 5°. The low standard deviations in these measurements indicate that the wave field was uniform and not subject to local wind or current conditions. From east to west (downtrack) the direction of propagation rotated slightly counterclockwise.

As examined in numerous studies, critical nonlinearities can occur in SAR imagery of ocean waves when the waves are propagating in the azimuth or parallel direction with respect to the flight path of the SAR platform [e.g., *Alpers*, 1983; *Alpers and Bruening*, 1986; *Beal et al.*, 1986; *Monaldo and Lyzenga*, 1988]. With this geometry, velocity bunching is the dominant SAR wave-imaging mechanism. Essentially, orbital velocities of the wave facets in the radial direction produce varying Doppler displacements within the moving SAR beam which tend to group (bunch) and spread the locations of the wave-scattering elements in the azimuth direction on the image map. For ocean swell, there is generally no distortion or weak distortion in the mapping. Distortion in the position of the facets is aggravated by increasing satellite altitude and by fully developed and fetch-limited wind seas and swell with large wave height, which results in nonlinear mapping and an apparent reduction of energy in the azimuth direction. As mentioned earlier in section 4, when waves are propagating into an ice field, the high-frequency wave scatterers are damped out effectively by the frazil ice [*Martin and Kauffman*, 1981], and the waves can be imaged by SAR because of the velocity-bunching mechanism and without distortion [*Lyzenga et al.*, 1985].

One model for estimating the transition from linearity to nonlinearity for fully developed wind waves propagating in the azimuth direction was defined by *Alpers* [1983]. For a linearity parameter $\mathbf{c}$, significant nonlinearities occur if $\mathbf{c} > \pi/2$, resulting in the spectral peaks shifting toward lower azimuthal wave numbers. For Seasat the linearity parameter $\mathbf{c}$ becomes

$$\mathbf{c} = 1.6 \times 10^3 \cos \alpha \lambda_d^{-3/2} H_s \tag{24}$$

where λ_d is the dominant measured wavelength and α is the azimuth angle. For this study, using $\alpha = 35°$, $\lambda_d = 181$ m, and $H_s = 4.5$ m, $\mathbf{c} = 2.42$, which would again indicate significant nonlinearity. *Alpers* [1983] and *Alpers and Bruening* [1986] both state that nonlinearities in swell are much weaker than for fully developed wind waves because the ratio $H_s/\lambda_d{}^{3/2}$ is smaller for swell and the width of the swell spectrum is narrower than for a Pierson-Moskowitz spectrum. The result would be that the shift toward lower azimuthal wave numbers for swell would occur at larger values of $\mathbf{c}$ as compared with wind waves. For the case of wind waves propagating at an intermediate angle between azimuth and range directions, only a slight change in wavelength occurs, but there is a shift in the apparent wave direction toward range that is significant. However, this effect decreases with increasing wavelength. In summary, this study indicates that the dominant waves visible in the imagery are swell, not wind waves. It is now left to examine the shape of the wave spectra for any indications of azimuth falloff.

Examples of the wave spectra for open ocean subscenes are shown in Figure 7. For box 1 the spectrum shows a well-defined narrow-banded dominant peak propagating northwest and a lower-frequency peak aligned north-south. The spectrum for box 30 is very similar in appearance (not shown). Boxes 1 and 30 have wavelengths of 179 m and 181 m and directions of 299° and 292°, respectively. There is no indication of a decrease in energy in the azimuth direction in either spectrum. The lower-frequency peak in box 1 has a direction of 359°, which is nearly normal to the wind direction and the alignment of the ice bands that appear near the ice-ocean margin. This indicates that the low-frequency peak may be caused by the presence of Langmuir cells or windrows in the open ocean [*Gerling*, 1986]. The appearance of the two peaks does not match the nonlinear harmonics seen in spectra described by *Bruening et al.* [1988]. As the dominant waves in these two spectra are narrow-banded and are not aligned with the local wind, a preliminary conclusion would be that the waves are swell and are not being altered in appearance because of nonlinearities arising from velocity bunching.

However, the spectra for the remaining ocean boxes 5, 9, 14, and 19 have different appearances. The dominant wave peaks are clearly seen in boxes 5, 9, and 14 and less so in box 19 (Figure 7), but, as is seen in box 19, each of these spectra contains more broad-banded, omnidirectional frequency distributions than the narrow-banded swell seen in boxes 1 and 30. One possible explanation for the wider frequency and directional distribution is that less energetic components of the wave field are being reflected by the ice in many directions since the angles of the incoming waves would be highly variable because of the undulating ice edge. Another possible explanation is that there are local differences in the wave field caused by varying local wind conditions.

Curiously, although there is indication of the presence of waves with a direction and wavelength similar to that of the measured dominant wave component, no clear peaks were detected in ocean box 24. This box also showed a reduction in the frequency distribution toward lower wave numbers. An investigation into this discrepancy was performed by altering the parameters used in the peak-finding routine [*Holt et al.*, 1990] in an attempt to resolve this wave component, but to no avail.

In box 19 (Figure 7) there is some indication of a reduction in the frequency response in the azimuth direction. The wavelength cutoff is at about 150 m, which is shorter than the dominant measured wavelength. However, if the waves were subject to nonlinearities due to velocity bunching, the waves would be rotated toward the range direction and/or would become longer in wavelength. As indicated in Figure 7, while the wavelength for box 19 is slightly longer than for boxes 1 and 30 (187 m, compared to 179 m and 181 m, respectively), the wave direction for box 19 is actually rotated toward the azimuth direction as compared to boxes 1 and 30.

In conclusion, on the basis of the observations made above, namely, (1) the clear appearance of narrow-banded wave peaks in boxes 1, 5, 9, 14, and 30 and (2) the steady rotation of the waves toward the azimuth, rather than range, direction from lines A–E, the dominant wave components detected in the open ocean wave spectra are indeed swell and are not subject to nonlinearities due to velocity bunching.

6.3. *Results of Wave Measurements in the Ice*

Within the ice the dominant wave peaks are generally narrow-banded with almost no other frequency components present. This is clearly seen in boxes 3, 4, and 20–23 in Figure 7. Detectable peaks in the boxes containing frazil ice were obtained from boxes 2, 15, and 27 but not in boxes 10, 25, and 26 (Table 1). Note that for these latter three boxes the mean brightness values were generally very low, indicating that the backscatter levels were approaching the system noise floor. Peaks were clearly detectable in all remaining boxes containing ice. From these spectra it is very evident that the ice field has effectively reduced all high-frequency wave components through damping and/or reflection.

The development of the dominant spectral peak in the ice along lines A–E (boxes 1–23) is shown schematically in Figure 8, separated by wavelength and angle. Most of this analysis will focus on lines A–E since line F did not resolve detectable peaks in the ocean and frazil ice (boxes 24–26). For line F, only the inner boxes (27–29) in the pancake ice gave clearly peaked spectra. As Table 1 shows, the reduced wavelengths in these boxes are very similar to wavelengths observed in lines A–E at the same penetrations.

Each line of measurements shows a sharp decrease in wavelength from the open ocean (mean wavelength of 181 m) to a distance of 30–40 km into the ice field with less change occurring over the remaining approximately 25 km (Figure 8). Lines A–D are fairly similar, but line E has the sharpest decrease to 25 km followed by the smallest change over the remaining distance. This variation in the reduction of wavelength is illustrated by considering the measurements in intervals of distance. At the distances between 20 and 30 km the mean wavelength is 163 m with a standard deviation of 5 m. Between 35 and 45 km the mean wavelength is 157.5 m with a very low standard deviation of 1.2 m. From 45 to 55 km the mean wavelength is 153 m with a standard deviation of 4.3 m. Finally, the two measurements beyond 60 km are both 149.5 m. These measurements indicate a slightly more rapid reduction of wavelength over the outermost ice margin and a more gradual reduction over the remainder of the visible ice field. The total change in wavelength from 181 m to 150 m represents a reduction of 18% over 65 km. These changes are significant when compared to the estimation error of ±5% in wavelength.

Another way to assess the change in dispersion is to consider the net change in wavelength from the ocean to the last measurement in each line. The net change in wavelength for line A is 22.6 m, for line B is 24.0 m, for line C is 27.7 m, for line D is 30.4 m, and finally for line E is 37.6 m. When normalized by distance, these changes become 0.396, 0.516, 0.524, 0.465, and 0.589 m km^{-1}, respectively. These measurements indicate that there is a trend toward a more rapid change in wavelength from line A to line E.

The change in wave propagation direction over distance is apparent but to a lesser degree than in wavelength (Figure 8). From line A to line E there is also a gradual rotation in the incoming waves of more than 15° toward the south (counterclockwise), as was found in the previous section with the ocean measurements. Within the ice, lines A–C show a counterclockwise rotation over distance, but lines D and particularly E exhibit little rotation. The net change in rotation for line A is 9°, for line B is 12°, for line C is 14°, for line D is 5°, and for line E is less than 0.5°. The estimation error in propagation angle is ±2°, but the overall trends in the measurements indicate that actual angular rotation took place.

6.4. *Derivation of Ice Type Information*

The mean and standard deviation of the brightness values for subscenes 1–30 are shown in Figure 9*a*. The brightness values fall into five clearly isolated clusters, especially for ocean and frazil ice, which closely match the image interpretation of the new ice types in section 5. Three classes of pancake ice can be qualitatively separated by clustering on the basis of both increasing mean and standard deviation brightness levels, which correspond in general to increasing distance into the new ice zone. As mentioned earlier, these three classes indicate increasing roughness in the pancake ice possibly due to increasing concentration and/or cake size. There is perhaps not as clear a distinction between classes 3 and 4 of the pancake ice as with the other three classes. However, the brightest classes (4 and 5) come from the easternmost subscenes (lines A–C), which contain no class 3 ice, while the western subscenes (lines D–F) contain only class 3 ice except for one class 4 subscene (box 18). This distinction in type of pancake ice between the western and eastern portions of the two images was pointed out in a relative sense in section 5.

Figure 9*b* shows the five ice classes plotted by wavelength. There is a clear decrease in wavelength from ocean to frazil to pancake ice. Interestingly, the measured wavelengths in class 4 have a wider range and slightly higher mean value than those in classes 3 and 5. However, except for box 18, classes 4 and 5 occur together in lines A–C and still show a clear decrease in wavelength when considered separately from class 3. The measured wavelengths in classes 3 (lines D–F) and 5 (lines A–C) are essentially the same, indicating that the apparent difference in roughness or condition between these classes is not significant enough to produce changes in the wave dispersion based on varying brightness in the types of pancake ice.

7. COMPARISON OF MEASUREMENTS WITH THEORY

The results shown in Figure 8 and Table 1 clearly agree in a qualitative sense with the theoretical model developed in section 3. First, the fact that the wind is directed toward the ice implies that the thickness of the frazil ice slick should increase with increasing penetration; this has been observed in every case of a frazil ice slick being wind-herded against a downwind boundary of thicker ice [*Martin and Kauffman*, 1981]. The transition in the nature of the image from a dark return characteristic of frazil ice to a bright return characteristic of the raised edges of pancake ice is also typical of this behavior, since frazil turns into pancake when under compression in a wind and wave field [*Martin and Kauffman*, 1981]. Given that the ice is thickening with increasing penetration, we expect from (10) that the wavelength of a given spectral component will decrease with

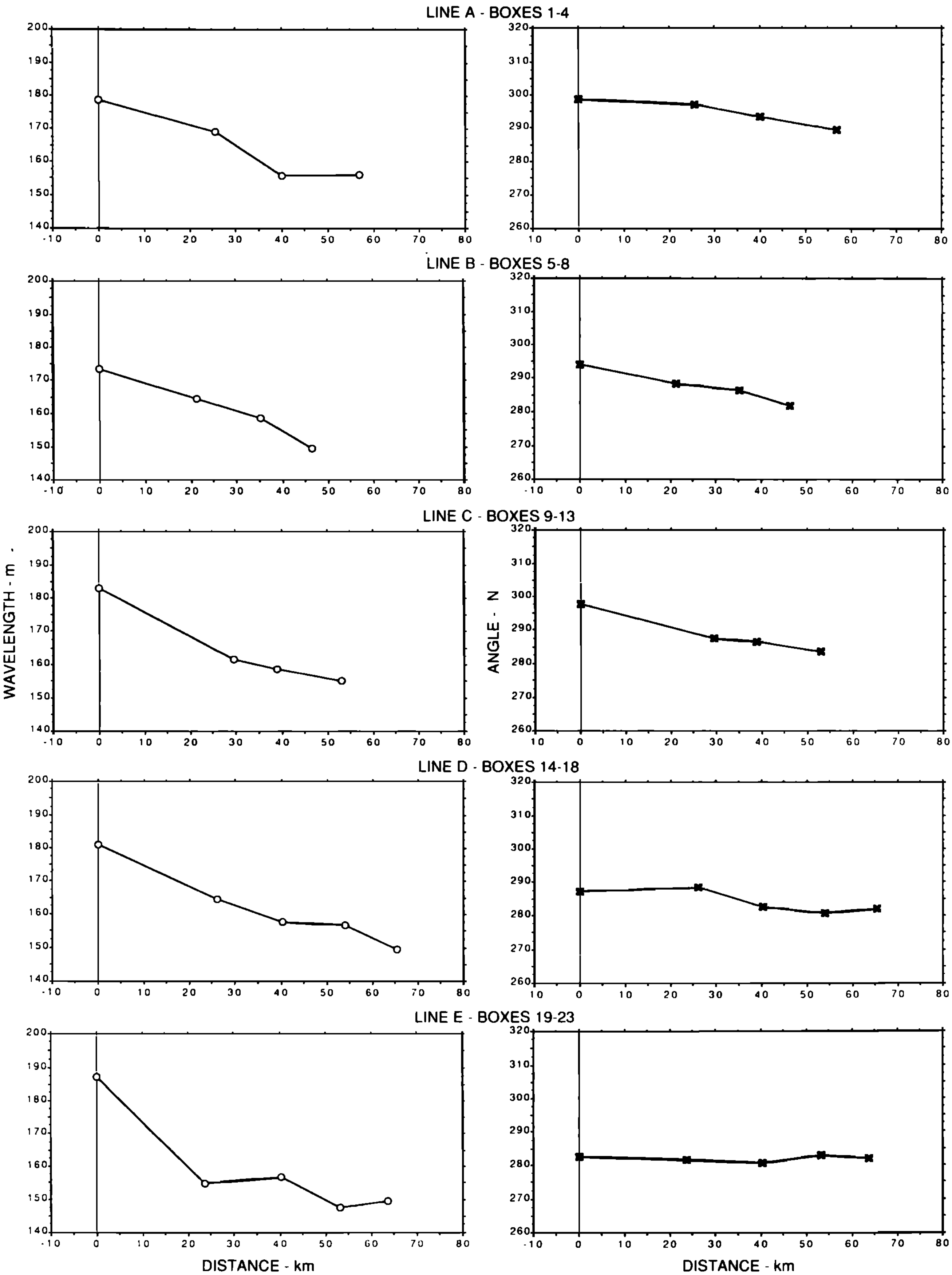

Fig. 8. (Left) Wavelength and (right) direction of the main spectral component along lines A–E as derived from the wave spectral contour plots.

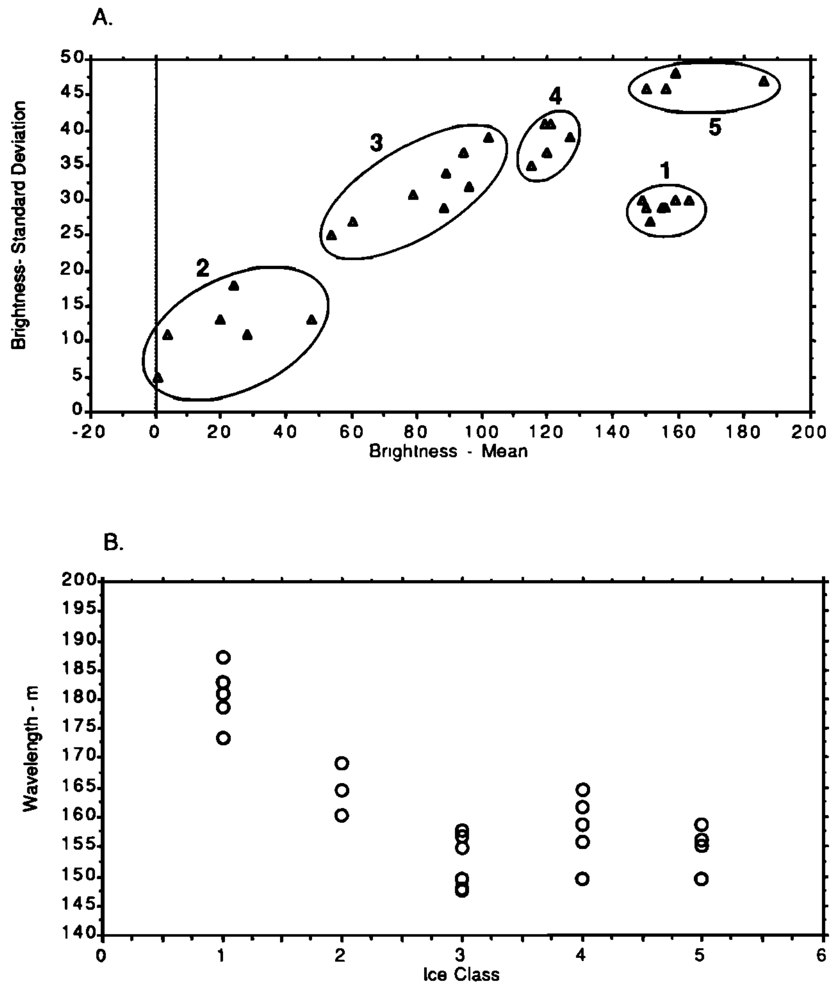

Fig. 9. (*a*) The mean and standard deviation of image brightness for each subscene (boxes 1–30). The intensity range is from zero to 256. Class 1 is the open ocean. Class 2 is frazil ice. Classes 3–5 are pancake ice with increasing brightness. (*b*) The wavelength measurements for each of the five classes of ocean and ice types are also shown.

increasing penetration. This is in fact what is observed. Finally, by Snell's law this progressive decrease in wavelength should be accompanied by a refraction toward the normal, where "normal" is defined as the direction of maximum gradient in ice thickness. We observe progressive refraction in the same sense in four of the five lines shown in Figure 8.

Alternative explanations for the wavelength change and refraction are (1) that the change in wavelength with increasing penetration is due to a change in the dominant wave period within the spectrum, rather than to a change in the wavelength of a single spectral component; (2) bathymetric effects; or (3) local current gradients.

Bathymetry may well be significant, as the image is situated over the East Siberian Shelf. As can be seen from Figure 6*c*, water depths within the image area lie in the range 40–80 m. This is sufficient to produce a decrease in wavelength for the wave of dominant period relative to its wavelength in deep water. For a wave of an observed wavelength of 180 m the decreases for water depths of 50 m, 60 m, and 70 m are 9, 5, and 2 m, respectively. Line A appears to lie over water of depth about 70 m, lines B and C lie over 60 m, and lines D and E lie over 40–50 m. However, it can be seen from the bathymetric curves that the direction of each line is approximately the same as the direction of the isobaths in the region, so that water depth along each line remains fairly steady. We therefore do not expect significant along-line wavelength changes due to bathymetry alone.

The local currents in the region are largely unknown since current measurements in the Chukchi Sea are sparse. As described by *Coachman et al.* [1975], the upper layer currents near Herald Canyon are about 20 cm s^{-1} at directions north/northwest. For significant wave refraction to occur because of current interaction, the incident angle of the incoming waves with respect to the current direction must be less than 45° or greater than 135°, where reflection occurs at even small current shears [*Phillips*, 1981]. For the measured wave directions this would require the current to be flowing mostly parallel to the wave field (east/west). For significant changes in wavelength to occur because of current interaction, the incoming wave field must be normal to the current direction (southwest/northeast) and have a significant current shear which increases toward the ice field, in this case. The occurrence of substantial current shears appears to be unlikely. The two situations required for significant changes in direction and wavelength are in fact opposing. In summary, while we cannot discount any effects due to local

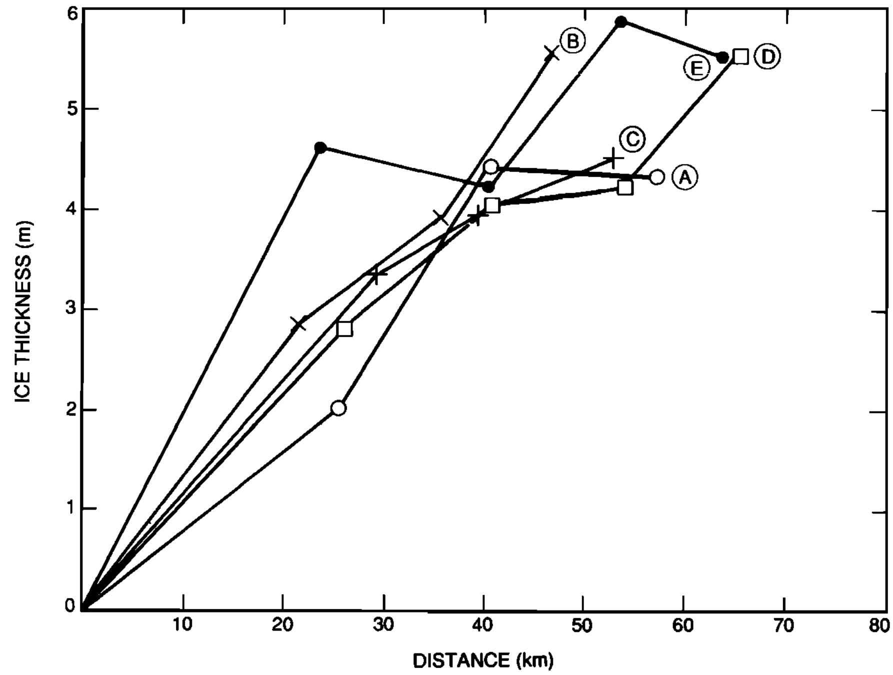

Fig. 10. Equivalent ice thickness *ch* as a function of distance into the ice for lines A to E, calculated from wavelength changes.

currents, the current conditions needed for these changes appear unlikely to exist.

A change in dominant wave period toward a shorter period, which would give a shorter wavelength in the absence of ice effects, is the opposite of what is normally observed in ice fields composed of larger floes [e.g., *Wadhams et al.*, 1988] where scattering preferentially attenuates shorter-period waves or in frazil slicks on a laboratory scale [*Martin and Kauffman*, 1981] where viscous processes act in the same sense. Therefore, if anything, we would expect the dominant wave period to increase with increasing penetration, and the real decrease in wavelength for a given spectral component may thus be even greater than that observed.

We will assume for the purposes of further discussion that the wavelengths and angles in Figure 8 refer to a single spectral component for each line.

In drawing quantitative conclusions, it is most fruitful to deal with the wavelength data, since these data can be related very easily to ice thickness. Equation (10) can be rearranged to give

$$ch = (\lambda - \lambda_i)\rho_w/2\pi\rho_i = 0.1768(\lambda - \lambda_i) \qquad (25)$$

if we assume that $\rho_i/\rho_w = 0.9$. Thus there is a simple linear relationship between equivalent ice thickness in the slick and wavelength change from open water to ice. In Figure 10 we have plotted the equivalent ice thickness calculated from (25) for each of lines A to E. Our assumption is that each of the open water wavelengths is an independent sample of a homogeneous wave field, so that rather than using individual values for λ, we use the averaged open water value, which in section 6.2 we found to be (180.7 ± 4.5) m. If we accept that the standard deviation of the open water wavelength is an appropriate value to apply to every wavelength (this is probably a pessimistic assumption, since Figure 8 shows little evidence of random fluctuations of this magnitude in the progression of wavelengths), then this would result in a standard deviation of 1.12 m in thickness values computed from wavelength differences.

The results of Figure 10 are not inconsistent with thicknesses to which frazil ice suspensions have been observed to grow in the polar regions. According to *Martin* [1981], thicknesses of up to 5 m have been seen. In our experimental situation we have a strong wind blowing at subzero temperatures over a wide open water region for at least 3 days prior to the observation. These are ideal circumstances for frazil ice to be generated on the ocean surface, herded toward a downwind obstacle, and piled up there to reach great thicknesses. It should be noted that the thicknesses calculated are equivalent thicknesses (*ch*) and that if the ice concentration in the suspension is low, the physical thickness of the slick would have to be unrealistically great. It is likely, however, that in a dense frazil suspension the interstitial water particles are isolated from the underlying ocean and hydrodynamically form part of the slick, so that we can assume that (*ch*) is close to *h*. The whole slick therefore behaves as a slurry as far as mass loading is concerned. Undoubtedly, the overall physics of wave propagation in frazil ice is more complex than this, since the viscous attenuation described by *Martin and Kauffman* [1981] is occurring simultaneously with the wavelength and amplitude changes due to mass loading. But, to a first approximation, we have shown that if the two mechanisms are separated, the effect of mass loading alone on wavelength can be seen as reasonably consistent with this set of observations, although the estimated thickness is still high given the temperature history of the region.

Thus we find in the quantitative data considerable support for the idea that our theoretical model has validity in the interpretation of SAR imagery of waves in frazil ice. This has been the first opportunity to test the theory against field data, since as yet there have been no conventional wave buoy measurements made within and across fields of frazil ice.

Any attempt to draw conclusions from the refraction data is hampered by our lack of independent knowledge of the direction of the maximum gradient in ice thickness. Nevertheless, some patterns are apparent in Figure 8, again tending to support the relevance of our theory. Line E shows little or no refraction and so can be assumed to lie in the direction of the maximum ice thickness gradient. A priori, we expect this gradient to lie approximately in the direction of the principal component of the wave field, since, as section 3.3 shows, this is the direction of the herding force due to wave radiation pressure. Line E also has the greatest gradient of wavelength change, again suggesting that ice thickness is increasing most rapidly along this axis. Lines A to D begin with incident angles which are rotated by up to 15° northward relative to E, and the gradient of wavelength decrease is least for line A where there is the greatest initial obliqueness of incident wave angle referenced to line E. Qualitatively, we can thus see that incoming waves are being refracted toward the normal, with the initial angle of incidence being indicated by the rate of wavelength decrease relative to that observed along the presumed ice thickness gradient (line E). We cannot go further than this as we cannot be sure that the ice thickness gradient lies in the same direction for each of the lines.

8. CONCLUSIONS

We have shown in this paper that a theory of wave propagation in fields of frazil and pancake ice, based on mass loading of the surface by the ice, yields predictions about wavelength changes in the ice field which are compatible with measurements made from Seasat SAR imagery. The theoretical prediction of a frequency limit for wave propagation in frazil ice also serves to explain why frazil ice appears dark in SAR imagery, since there is little or no energy present at the Bragg wavelength.

If we assume that the theory is valid, it provides us for the first time with a means of inferring sea ice thickness from SAR data. Although this method is applicable only to one specific ice type, the application may be a very useful and important one. In the Antarctic during early winter the advancing circumpolar ice edge has been found to consist of pancake ice up to a penetration of some 270 km [*Wadhams et al.*, 1987], making pancake ice an important component of the entire Antarctic ice field. In the Arctic, although pancake ice is not such an important component of the ice cover as a whole, it is thought to be the chief ice type within the "Odden" feature, a large ice tongue in the Greenland Sea which can appear and disappear within a few days during winter. In both cases the advent of the ERS 1 satellite will enable us to monitor these regions and use the results of this paper (confirmed, it is hoped, by in situ wave measurements) to derive ice thicknesses.

Acknowledgments. The authors would like to thank Ron Kwok and Joanne Shimada of JPL for their efforts in the generation of the wave products; Mark Drinkwater and Frank Carsey, JPL, for insightful discussions; and Harry Stern of the Applied Physics Laboratory at the University of Washington for the Navy surface analysis. This work was performed at SPRI with support from the Office of Naval Research, Arctic Program (P.W.) and at the Jet Propulsion Laboratory, California Institute of Technology, under contract with the National Aeronautics and Space Administration (B.H.).

REFERENCES

Alpers, W. R., Monte Carlo simulations for studying the relationship between ocean wave and synthetic aperture radar image spectra, *J. Geophys. Res.*, *88*(C3), 1745–1759, 1983.

Alpers, W. R., and C. Bruening, On the relative importance of motion-related contributions to the SAR imaging mechanism of ocean surface waves, *IEEE Trans. Geosci. Remote Sens.*, *GE-24*, 873–885, 1986.

Armstrong, T., B. B. Roberts, and C. W. M. Swithinbank, Illustrated glossary of snow and ice, *Spec. Publ. 4*, 59 pp., Scott Polar Res. Inst., Cambridge, England, 1966.

Beal, R. C., T. W. Gerling, D. E. Irvine, F. M. Monaldo, and D. G. Tilley, Spatial variations of ocean wave directional spectra from the Seasat synthetic aperture radar, *J. Geophys. Res.*, *91*(C2), 2433–2449, 1986.

Bruening, C., W. Alpers, L. F. Zambresky, and D. G. Tilley, Validation of a synthetic aperture radar ocean wave imaging theory by the Shuttle Imaging Radar-B experiment over the North Sea, *J. Geophys. Res.*, *93*(C12), 15,403–15,425, 1988.

Carsey, F. D., and G. Pihos, Beaufort-Chukchi seas summer and fall ice margin data from Seasat: Conditions with similarities to the Labrador Sea, *IEEE Trans. Geosci. Remote Sens.*, *27*, 541–551, 1989.

Carsey, F. D., S. A. Digby-Argus, M. J. Collins, B. Holt, C. E. Livingstone, and C. L. Tang, Overview of LIMEX'87 ice observations, *IEEE Trans. Geosci. Remote Sens.*, *GE-27*, 468–482, 1989.

Coachman, L. K., K. Aagaard, and R. B. Tripp, *Bering Strait: The Regional Physical Oceanography*, 172 pp., University of Washington Press, Seattle, 1975.

Fu, L.-L., and B. Holt, Seasat views oceans and sea ice with synthetic aperture radar, *Publ. 81-120*, 200 pp., Jet Propul. Lab., Pasadena, Calif., 1982.

Gerling, T. W., Structure of the surface wind field from the Seasat synthetic aperture radar, *J. Geophys. Res.*, *91*(C2), 2308–2320, 1986.

Gow, A. J., S. F. Ackley, W. F. Weeks, and J. W. Govoni, Physical and structural characteristics of Antarctic sea ice, *Ann. Glaciol.*, *3*, 113–117, 1982.

Holt, B., R. Kwok, and J. Shimada, Ocean wave products from the Alaska SAR Facility Geophysical Processor System, paper presented at Inernational Geoscience and Remote Sensing Symposium (IGARSS'90), Inst. of Elect. and Electron. Eng., College Park, Md., May 20–24, 1990.

Johannessen, O. M., J. A. Johannessen, J. Morison, B. A. Farrelly, and E. A. S. Svendsen, Oceanographic conditions in the marginal ice zone north of Svalbard in early fall 1979 with an emphasis on mesoscale processes, *J. Geophys. Res.*, *88*(C5), 2755–2769, 1983.

Keller, J. B., and M. Weitz, Reflection and transmission coefficients for waves entering or leaving an icefield, *Commun. Pure Appl. Math.*, *6*, 415–417, 1953.

Lange, M. A., S. F. Ackley, G. S. Dieckmann, H. Eicken, and P. Wadhams, Development of sea ice in the Weddell Sea Antarctica, *Ann. Glaciol.*, *12*, 92–96, 1989.

Liu, A. K., B. Holt, and P. W. Vachon, Wave propagation in the marginal ice zone: Model predictions and comparisons with buoy and synthetic aperture radar data, *J. Geophys. Res.*, *96*(C3), 4605–4621, 1991.

Longuet-Higgins, M. S., The mean forces exerted by waves on floating or submerged bodies with applications to sand bars and wave power machines, *Proc. R. Soc. London, Ser. A*, *352*, 463–480, 1977.

Lyzenga, D. R., R. A. Shuchman, J. D. Lyden, and C. L. Rufenach, SAR imaging of waves in water and ice: Evidence for velocity bunching, *J. Geophys. Res.*, *90*(C1), 1031–1036, 1985.

Martin, S., Frazil ice in rivers and oceans, *Annu. Rev. Fluid Mech.*, *13*, 379–397, 1981.

Martin, S., and P. Kauffman, A field and laboratory study of wave damping by grease ice, *J. Glaciol.*, *27*(96), 283–313, 1981.

Mollo-Christensen, E., Interactions between waves and mean drift in an ice pack, *J. Geophys. Res.*, *88*(C5), 2971–2972, 1983.

Monaldo, F. M., The consequences of sampling variability on the estimation of wave number and propagation direction from spaceborne SAR image spectra, *IEEE Trans. Geosci. Remote Sens.*, *GE-29*, 113–119, 1991.

Monaldo, F. M., and D. R. Lyzenga, Comparison of Shuttle Imaging Radar-B ocean wave spectra with linear model predictions based on aircraft measurements, *J. Geophys. Res.*, *93*(C12), 15,374–15,388, 1988.

Perry, P. K., and H. S. Fleming, Bathymetry of the Arctic Ocean, *Map and Chart Ser. MC-56*, Geol. Soc. of Am., Boulder, Colo., 1986.

Peters, A. S., The effect of a floating mat on water waves, *Commun. Pure Appl. Math.*, *3*, 319–354, 1950.

Phillips, O. M., The structure of short gravity waves on the ocean surface, in *Spaceborne Synthetic Aperture Radar for Oceanography*, edited by R. C. Beal, P. S. DeLeonibus, and I. Katz, pp. 24–31, Johns Hopkins Press, Baltimore, Md., 1981.

Raney, R. K., P. W. Vachon, R. A. DeAbreu, and A. S. Bhogal, Airborne SAR observations of ocean waves penetrating floating ice, *IEEE Trans. Geosci. Remote Sens.*, *GE-27*, 492–500, 1989.

Shapiro, A., and L. S. Simpson, The effect of a broken ice field on water waves, *Eos Trans. AGU*, *34*(1), 36–42, 1953.

Sutherland, L. L., R. A. Shuchman, P. Gloersen, J. Johannessen, and O. Johannessen, SAR and passive microwave observations of the Odden during MIZEX '87, in IGARSS'89 12th Canadian Symposium on Remote Sensing, *IEEE Publ. 89CH2768-0*, pp. 1539–1544, Inst. of Elect. and Electron. Eng., New York, 1989.

Tsang, G., and T. O. Hanley, Frazil formation in water of different salinities and supercoolings, *J. Glaciol.*, *31*(108), 74–85, 1985.

Wadhams, P., M. A. Lange, and S. F. Ackley, The ice thickness distribution across the Atlantic sector of the Antarctic Ocean in midwinter, *J. Geophys. Res.*, *92*(C13), 14,535–14,552, 1987.

Wadhams, P., V. A. Squire, D. J. Goodman, A. M. Cowan, and S. C. Moore, The attenuation rates of ocean waves in the marginal ice zone, *J. Geophys. Res.*, *93*(C6), 6799–6818, 1988.

Weitz, M., and J. B. Keller, Reflection of water waves from floating ice in water of finite depth, *Commun. Pure Appl. Math.*, *3*, 305–318, 1950.

B. Holt, Jet Propulsion Laboratory, California Institute of Technology, 4800 Oak Grove Drive, Pasadena, CA 91109.

P. Wadhams, Scott Polar Research Institute, University of Cambridge, Lensfield Road, Cambridge CB2 1ER, England.

(Received August 28, 1990;
revised December 3, 1990;
accepted November 9, 1990.)